Journal of Structural Geology, Vol. 14, No. 4, pp. 437 to 449, 1992
Printed in Great Britain

0191-8141/92 $05.00+0.00

Stresses beneath a ramping thrust sheet

DOUGLAS GOFF* and DAVID V. WILTSCHKO

Department of Geology and Center for Tectonophysics, Texas A&M University, College Station, TX 77841-3113, U.S.A.

(*Received* 18 *March* 1991; *accepted in revised form* 9 *October* 1991)

Abstract—There is a systematic progression of both the timing of motion of thrust sheets and the spacing of thrust ramps during the development of some thrust-dominated foreland fold-and-thrust belts. On the basis of these observations, we suggest that a regional mechanical process that controls frontal ramp formation may dominate local effects such as stratigraphic pinchouts and interaction with basement. To investigate this process we have developed elastic, plane strain models of the state of stress in the footwall of the last formed, or most forward thrust ramp. These models include the load of an overriding thrust sheet and a synorogenic sedimentary cover. The effect of emplacing a thrust sheet or developing a synorogenic sedimentary cover above an incipient thrust sheet is to stabilize the footwall toward the hinterland with respect to failure, and thereby move failure more to the foreland. Failure is localized where there is a favorable trade-off between the spatial rates at which mean stress and differential stress decrease toward the foreland. The models also predict that frontal ramps nucleate well above the basal décollement and propagate upward and downward eventually linking with the regional décollement. Fault trajectories predicted by using a Coulomb criterion are subhorizontal in the hinterland portion of the model and curve upward to the foreland resulting in a curved 'flat and ramp' geometry. These analyses show that each successive thrust sheet would be thinner, as well as shorter, than the previous thrust sheet. Based on these results, we propose a model for the formation of the first 'thin-skinned' thrust sheet in the external portions of orogenic belts. The synorogenic sediments that form during uplift of the internal zones of mountain belts will cover the preorogenic strata to the foreland. As deformation progresses to the foreland, and deformation becomes more shallow and more brittle in nature, the preorogenic strata will interact with the synorogenic strata and failure will occur creating the first 'brittle' thrust sheet. The location of this first thrust will be controlled by the mechanisms outlined in our models. To the foreland of this point, each sucessive thrust fault will localize as a result of the combined effects of an overriding thrust sheet and synorogenic deposits.

INTRODUCTION

Two features characterize the kinematics of thrust development. First, the time of major motion on the largest thrust faults within several foreland thrust belts becomes younger toward the craton (Rubey & Hubbert 1959, Armstrong & Oriel 1965, Bally *et al.* 1966, Jones 1971, Perry 1978, Wiltschko & Dorr 1983). Although there is apparently some coincidence in movement between several thrust sheets, geometric arguments within the Canadian Rockies suggest that thrust development was in general hinterland to foreland (Bally *et al.* 1966, Jones 1971). In other localities, however, dating of cross-cutting and overlapping relationships suggests that later thrust sheets moved only after the previous thrust had stopped (Wiltschko & Dorr 1983). Second, as thrust sheets stack up, their spacing (the across-strike length of thrust sheets measured as the restored distance between frontal ramps) decreases toward the foreland (Fig. 1) (see Goff 1990). The regularity both in timing and in spacing suggests that there is an identifiable mechanical control on thrust-sheet stacking.

We study the mechanics of imbrication of the footwall of the most forward (cratonward) thrust sheet in order to examine the initiation of the next thrust sheet in the sequence. We seek an explanation for the spacing of thrust fault ramps and insight into the initiation of new thrust faults. The stress regime in the footwall beneath a ramping thrust sheet is modelled by analytical elastic models. The boundary conditions used simulate an overriding thrust sheet and/or synorogenic sedimentation. These incorporate thrust sheet interaction and the roles of regional compression, gravity, and hydrostatic fluid pressures.

Previous work

Previous studies have treated the effect of variation in the stratigraphic section or in basement surface on ramp formation (Wiltschko & Eastman 1983, 1988, Woodward 1988). However, the areal distribution of irregularities appears to be neither systematic nor regular; as a result, there is no reason why these features would result in systematic imbrication over an entire foreland thrust belt. Woodward (1988) focuses primarily on stratigraphic changes and their effect on the location of lateral and frontal ramps. In his view facies variation is not a primary influence on frontal ramp development and thrust-ramp spacing. Modelling of the stresses above basement irregularities (Wiltschko & Eastman 1983, 1988) shows that stress concentrations are associated with these features, and may nucleate thrust faults. A basement effect on thin-skinned thrust faulting has been suggested in cross-sections drawn through several thrust belts (e.g. Jacobeen & Kanes 1974, 1975, Thomas 1985, Kraig *et al.* 1987, Schmidt & Perry 1988). However, the evidence provided by well constrained cross-sections through thrust belts reveals that the majority of thrust

*Present address: Exxon Production Research Company, P.O. Box 2189, Houston, TX 77252-2189, U.S.A.

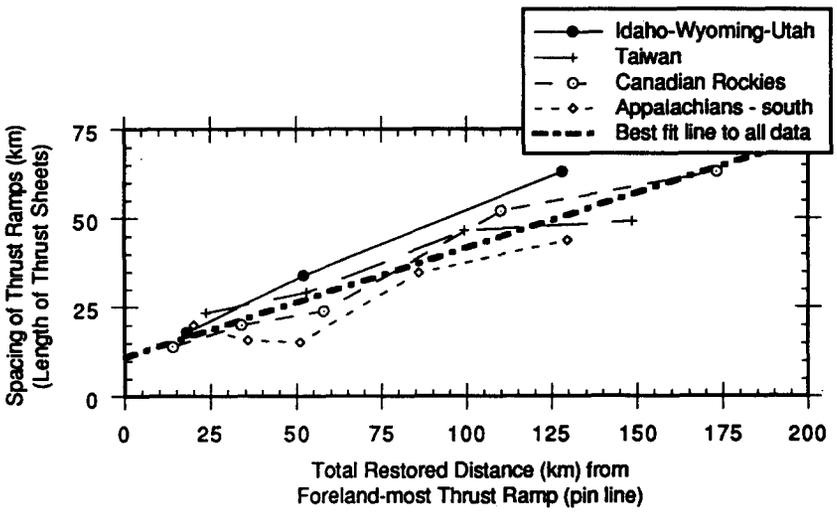

Fig. 1. Restored spacing of frontal ramps (length of thrust sheets) measured along the basal décollement from the most forward thrust ramp plotted vs the distance between thrust ramps. Measurements are made for thrust belts in which there is a general lack of complexity (duplexes and multiple levels of detachments within a single thrust sheet). Additionally, major thrusts are distinguished from minor or secondary 'break back' thrusts based on displacement and dating. Only major thrusts have been measured. Equation of best-fit line to all data is $Y = 11 + 0.307(X)$ with a correlation coefficient (R) of 0.925. Data from Dixon (1982, Idaho–Wyoming–Utah, cross-section 17); Suppe (1980, Taiwan); Woodward (1985, Appalachians, cross-section 22); Price (1981, Canadian Rockies).

ramps are locally unrelated to basement structures at depth (e.g. Suppe 1980, Dixon 1982, Lamerson 1982, Woodward 1985).

Only a few studies have dealt with the mechanics of thrust initiation and spacing. Mandl & Shippam (1981) model the imbrication within a thin thrust sheet. Their model consists of an elastic thrust sheet moving over a perfectly plastic weak décollement. Using a Coulomb failure criterion, failure is predicted to initiate at the lower hinterward corner of the thrust sheet and at the surface a short distance away from the upper hindward corner. The upper weak point is more pronounced in longer thrust sheets. The authors predict that long, thin thrust sheets are more apt to imbricate than short, thick sheets, and that this imbrication will proceed in a piggy-back manner from the hinterland to the foreland. Bombolakis (1986) represents a thrust sheet as a coupled oscillator with an average shear stress along the lower block of the coupled pair. The driving force for the system is the stress drop associated with repeated stick–slip events along the basal décollement. For a given stress drop, a rupture length along the basal décollement can be determined by using a relationship among the basal shear stress, mass, thickness and the topographic slope of the stratigraphic section above a new fault segment. This fault segment is the newly forming extension of the basal décollement. As a result of repeated stick–slip events along the new fault segment, the stratigraphic section at the foreland termination of the ruptured segment will experience repeated episodes of high strain that eventually lead to failure. The position within the stratigraphic section where failure initiates is a function of the elastic properties of the stratigraphic units. For the Hogsback (Darby) thrust of the Idaho–Wyoming–Utah thrust belt, Bombolakis (1989) argues that the thrust ramp initiated a significant distance above the décollement. From these two studies, he concludes that as the thickness of the stratigraphic cover decreases toward the foreland, the spacing between frontal ramps also will decrease. This relationship is observed in the Idaho–Wyoming–Utah thrust belt (Armstrong & Oriel 1965, Wiltschko & Dorr 1983), and in the central to southern Appalachians where the sedimentary cover thins along strike to the southwest (Kulander & Dean 1986). Platt (1988) uses a quasi-static force balance approach to model the development of the most forward frontal ramp in the Makran accretionary wedge in the Gulf of Oman. For most cases Platt limits the distance of emplacement of the overriding imbricate thrust sheet to the length of the thrust ramp. Platt concludes that small imbricate thrust sheets are possible, but rejects the possibility of long, thin thrust sheets. His analysis does not appear sufficiently general to be applied to thrust belts other than the one considered. Cello & Nur (1988) concentrate on the effect of fluid pressures on thrust plane rupture and ramp formation. They utilize a relationship developed by Pollard & Johnson (1973) to analyze the stress distribution around the upward bending of a stack of thin elastic plates (mode I opening). Cello & Nur apply this to a fault surface opening and lifting the rock above due to increased fluid pore pressures. They conclude that the length of the fault surface that would develop before ramping occurred would be approximately equal to the depth of the décollement, and that this length is equal to the final spacing between thrust ramps. This is not supported by observations within thrust belts (e.g. Dixon 1982, Woodward 1985). Finally, Panian & Pilant (1990) investigate the importance of topography on the state of stress at the leading edge of a thrust sheet. They solve for the stresses in a half space beneath a sloping surface. From their models they interpret that shear failure would initiate on a horizontal

plane at the level of the basal décollement within a broadly defined 'zone of high maximum shear stress'. This zone is located beneath the inflection in the surface slope, where the surface becomes horizontal. The new fault would propagate from this point upward to the foreland. Although Panian & Pilant recognize that high shear stress (high differential stress) is necessary to cause fracture, they ignore the effect of mean stress in determining where failure would initiate.

ANALYTICAL METHOD

The area of interest is in front of a ramping thrust sheet beneath the hanging wall and associated synorogenic sediments (Fig. 2) where the next thrust fault will form. This area is simplified by being placed in front of the ramp so that geometric complexities of an angled boundary are reduced. We have determined the stresses due to an overriding thrust sheet in three ways. All of the methods utilize Airy's stress function (φ) which satisifies the biharmonic equation

$$\frac{\partial^4\varphi}{\partial x^4} + 2\frac{\partial^4\varphi}{\partial x^2\partial z^2} + \frac{\partial^4\varphi}{\partial z^4} = 0. \quad (1)$$

In two of the methods, a stress state is found by selecting a stress function which yields appropriate stresses throughout the area of interest, using

$$\sigma_{xx} = \frac{\partial^2\varphi}{\partial z^2}; \qquad \sigma_{zz} = \frac{\partial^2\varphi}{\partial x^2}; \qquad \sigma_{xz} = -\frac{\partial^2\varphi}{\partial x\partial z}; \quad (2)$$

to find the stresses in the usual way (e.g. Timoshenko & Goodier 1970, pp. 31–33). In the third method, a distributed surface load is represented by point loads, the contribution of each being added up to yield the stress at any particular point in the body (e.g. Timoshenko & Goodier 1970, pp. 97–109).

The stresses associated with the overriding thrust sheet or synorogenic sedimentary cover result from the weight of the overburden and the shear stress along the interface between the overriding thrust sheet and the footwall. The overriding thrust sheet or synorogenic sedimentary cover above the model surface is considered mechanically detached from the footwall area. The overriding thrust sheet will not contribute to the regional compression, i.e. compression in the horizontal direction along the right and left boundaries of the model will not be imparted by the overriding thrust sheet. Tectonic compression is represented by an additional stress function which is added to that representing the overriding thrust sheet and/or synorogenic deposits. The stresses derived from these loads and the stresses associated with the gravity or the standard state of Anderson (1942) and Hafner (1951) are added to reach the final stress distribution. Finally, the effect of a hydrostatic pore pressure is considered.

Superposition of stress functions

To determine the total stress field due to all sources, we add three stress functions, with each contributing a different portion to the total stress system. The three portions of the total stress function are the stresses due to the gravitational standard state (φ_g), stresses due to the regional tectonic compression (φ_c) and the stresses due to the overriding thrust sheet (φ_t). The stress at any point in the model is the sum of the contributions from these three stress functions added on a term by term basis; e.g. $\sigma_{xx} = \sigma_{xx}(\varphi_g) + \sigma_{xx}(\varphi_c) + \sigma_{xx}(\varphi_t)$. The following derivations solve the stresses for each of these stress functions.

Standard state (φ_g)

The derivation for the stress state termed 'the standard state' by Anderson (1942) is given in detail in Hafner (1951). For this study we choose to use this simple depth relationship of vertical stress to depth so that: $\sigma_{xx} = \sigma_{zz} = -\rho g z$ and $\sigma_{xz} = 0$.

Solution for regional or tectonic compression (φ_c)

The stress function we choose for tectonic compression (φ_c) is

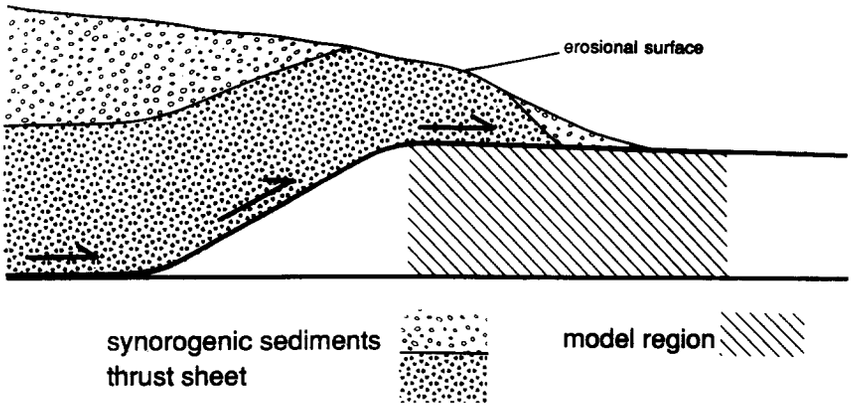

Fig. 2. Idealized geometry of thrust fault system, showing overlap of hanging wall and footwall and the development of a synorogenic sedimentary cover. The model area shown is the area of interest in the footwall for which stresses are determined. The effect of more hinterward piggy-back thrusts is ignored.

$$\varphi_c = \left(\frac{k}{2}\right)xz^2. \quad (3)$$

We desire a compression that is greatest at the origin of the model and decreases linearly to zero at $x = \pi$, where $x = \pi$ is the end of the area of interest (Fig. 3). Since the only portion of the total stress state attributable to equation (3) is regional compression, one of the boundary conditions is that the upper model surface ($z = 0$) is free of normal and shear stresses ($\sigma_{zz} = 0$, $\sigma_{xz} = 0$). By applying these boundary conditions the stresses are determined to be

$$\sigma_{xx} = kx; \quad \sigma_{zz} = 0; \quad \sigma_{xz} = -kz. \quad (4)$$

However, this will cause σ_{xx} to be a minimum at $x = 0$ and increase in the positive x direction (horizontal). For this model it is desirable to have σ_{xx} at its maximum at $x = 0$ and decrease to the foreland. Therefore, we define

$$k = \frac{-M}{\pi}, \quad (5)$$

where M is the maximum compression. Then, the stresses are

$$\sigma_{xx} = kx + M; \quad \sigma_{zz} = 0; \quad \sigma_{xz} = -kz. \quad (6)$$

Solution for overburden (φ_{t1}): exponentially thinning synorogenic sediments

The first approach models the overburden, an overriding thrust sheet and/or synorogenic deposits, as a mass that decreases in thickness exponentially toward the foreland (Fig. 3a). This is an 'end member' of possible geometries for the overriding thrust sheet–synorogenic sedimentary load, and it is consistent with the observation that clastic fan deposits can be approximated as point sources in which the volume of sediment decreases exponentially from the source (Wright & Coleman 1974, Lawrence *et al.* 1990). An appropriate stress function is

$$\varphi_{t1} = We^{-Sx}f(z); \quad (7)$$

where S is a scaling factor that controls the rate of decay of the height of the surface and W is an arbitrary constant. Equation (7) must satisfy the biharmonic equation, yielding

$$f(z) = A\sin(Sz) + B\cos(Sz) + Cz\sin(Sz) + Dz\cos(Sz). \quad (8)$$

By combining constants (e.g. $WA = A$) and using equations (2), the stresses are

$$\sigma_{xx} = e^{-Sx}\{-AS^2\sin(Sz) - BS^2\cos(Sz) + C[2S\cos(Sz) - S^2z\sin(Sz)] - D[2S\sin(Sz) + S^2z\cos(Sz)]\}; \quad (9a)$$

$$\sigma_{zz} = S^2e^{-Sx}\{A\sin(Sz) + B\cos(Sz) + Cz\sin(Sz) + Dz\cos(Sz)\} \quad (9b)$$

$$\sigma_{xz} = Se^{-Sx}\{AS\cos(Sz) - BS\sin(Sz) + C[Sz\cos(Sz) + \sin(Sz)] + D[\cos(Sz) - Sz\sin(Sz)]\}. \quad (9c)$$

The first boundary condition we use to constrain this problem is to set the vertical stress distribution along the surface $z = 0$ equal to the weight of the overburden. Since the synorogenic sedimentary cover is a maximum at $x = 0$, the vertical stress (σ_{zz}) at this point will also be a maximum, decreasing exponentially toward $x = \pi$. Therefore,

$$\sigma_{zz} = P_te^{-ax}; \quad (10)$$

where $P_t = \rho g H_t$, H_t is the height of the overburden at $x = 0$, $z = 0$, and a is the rate at which the height of the toe decreases with x. From equation (9b) evaluated at $z = 0$

$$\sigma_{zz} = P_te^{-ax} = S^2e^{-Sx}B. \quad (11)$$

Therefore,

$$B = \frac{P_t}{S^2}. \quad (12)$$

Another boundary condition relates the shear stress along the upper surface ($z = 0$) to the vertical normal stress ($\sigma_{xz} = \mu\sigma_{zz}$), a basic form of Amonton's Law. By using this boundary condition we find that

$$D = \mu\frac{P_t}{S} - AS. \quad (13)$$

This solution does not include the regional or tectonic compression, which are accommodated by the stress function (φ_g). Therefore, at $x = 0$ and $z = 0$, we set $\sigma_{xx} = 0$. Substituting this relationship into equation (9a) yields

$$C = \frac{P_t}{2S}. \quad (14)$$

Finally, at some level in a thrust belt, such as the décollement horizon or within the structural basement,

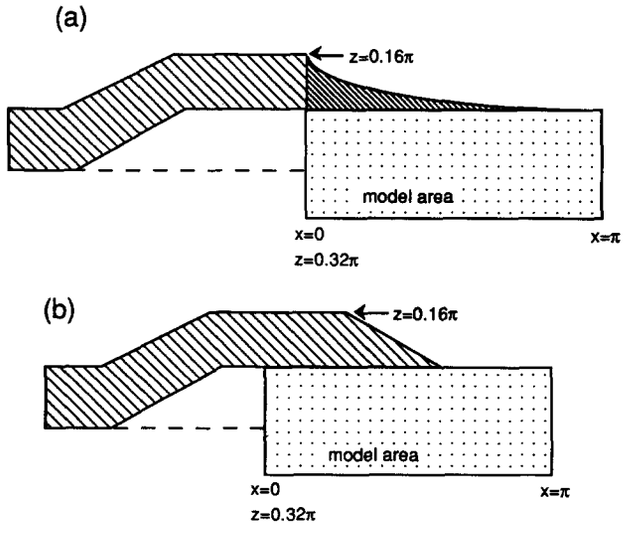

Fig. 3. Geometric representation of the surface loads for the models derived. (a) An exponentially decreasing surface load which simulates a point source of sedimentation. (b) An idealized fault-bend fold geometry to represent an overriding thrust sheet.

there is a plane of no vertical displacement. By choosing this plane as $z = \pi/2S$, and by using the method of images about this plane, we find that $D = 0$. These relationships (equations 12–14) can now be substituted into equation (9) to solve for the stress state, and then added to the stress functions for gravity and tectonic compression to yield

$$\sigma_{xx} = e^{-Sx}P_t\left\{-\mu\sin(Sz) - \frac{S}{2}z\sin(Sz)\right\} + kx + M - \rho g z; \quad (15a)$$

$$\sigma_{zz} = e^{-Sx}P_t\left\{\mu\sin(Sz) + \cos(Sz) + \frac{S}{2}z\sin(Sz)\right\} - \rho g z; \quad (15b)$$

$$\sigma_{xz} = e^{-Sx}P_t\{\mu\cos(Sz) + \tfrac{1}{2}[Sz\cos(Sz) - \sin(Sz)]\} - kz. \quad (15c)$$

Solution for overriding thrust sheet (φ_{t2}): fault-bend fold—Fourier series solution

Another 'end member' geometry of the load above a forming thrust sheet is that of a thrust toe without synorogenic sediments. This is represented in our models as a fault-bend fold (Fig. 3b). Since this geometric form does not have a mathematically continuous function, it is approximated by a Fourier series (Appendix).

The appropriate stress function consists of two parts:

$$\varphi_{t2} = \varphi_a + \varphi_b; \quad (16a)$$

where

$$\varphi_a = \kappa a_0\left(\frac{x^2}{2} - \mu x z\right), \quad (16b)$$

$$\varphi_b = \sum_{n=1}^{\infty} a_0\left[\frac{a_n}{n^2}\cos(nx) - \frac{b_n}{n^2}\sin(nx)\right]f(z). \quad (16c)$$

These two equations are the first two terms of the Fourier series representation of the geometry of the fault-bend fold. By application of the biharmonic equation, f(z) is found to be of the form

$$f(z) = \sum_{n=1}^{\infty}[E\cosh(nz) + F\sinh(nz) + Gz\cosh(nz) + Hz\sinh(nz)]. \quad (17)$$

Rewriting in terms of exponentials, adding $\varphi_a + \varphi_b$, and determining the stresses from equations (2) we find

$$\sigma_{xx} = 0 + \sum_{n=1}^{\infty}\left[\frac{a_n}{n^2}\cos(nx) - \frac{b_n}{n^2}\sin(nx)\right] \cdot \{E[n^2e^{nz}] + F[2ne^{nz} + zn^2e^{nz}] + G[n^2e^{-nz}] + H[-2ne^{-nz} + zn^2e^{-nz}]\}; \quad (18a)$$

$$\sigma_{zz} = \kappa a_0 + \sum_{n=1}^{\infty}[a_n\cos(nx) + b_n\sin(nx)] \cdot \{[E + Fz]e^{nz} + [G + Hz]e^{-nz}\}; \quad (18b)$$

$$\sigma_{xz} = \mu\kappa a_0 + \sum_{n=1}^{\infty}\left[\frac{a_n}{n}\sin(nx9) - \frac{b_n}{n}\cos(nx)\right] \cdot \{E[ne^{nz}] + F[e^{nz} + zne^{nz}] - G[ne^{-nz}] + H[e^{-nz} - zne^{-nz}]\}. \quad (18c)$$

The boundary conditions chosen to constrain this problem are similar to those used in the exponentially thinning sedimentary load model. First we require that at $z = \infty$ the effect of topography diminishes so that the vertical stress due to loading at the surface ($z = 0$) is zero. To approximate this, the vertical stress will be set equal to the constant κa_0 at $z = \infty$. This is a good approximation since at great depths stresses due to gravity will be much greater than the value of κa_0. Therefore, for φ_{t2} at $z = \infty$,

$$\sigma_{zz} = \kappa a_0 + \sum_{n=1}^{\infty}[a_n\cos(nx) + b_n\sin(nx)] \cdot [(E + Fz)e^{n\infty}] = \kappa a_0. \quad (19)$$

For this to hold E and F must be zero.

We further constrain the vertical stress along the surface to be the weight of the overburden (P_t) at $x = 0$:

$$\sigma_{zz} = \kappa a_0 + \sum_{n=1}^{\infty}[a_n\cos(nx) + b_n\sin(nx)] \cdot [-G] = P_t. \quad (20)$$

By inspection, we see that $\kappa = P_t = G$. Finally, horizontal compression (σ_{xx}) is set equal to zero at $x = 0$, $z = 0$. For this condition we find

$$\sigma_{xx} = \sum_{n=1}^{\infty}\left[\frac{-a_n}{n^2}\right] \cdot \{n^2G - 2nH\} = 0. \quad (21)$$

Therefore, $H = nG/2 = nP_t/2$. Since the constants G and H are now solved for in terms of P_t (the maximum vertical load), these expressions may be substituted into equations (18) to solve for the stresses. Finally, adding the components of stress to the tectonic load and gravity we find

$$\sigma_{xx} = 0 + \sum_{n=1}^{\infty}\left[\frac{a_n}{n^2}\cos(nx) - \frac{b_n}{n^2}\sin(nx)\right]P_t\left\{[n^2e^{-nz}] + \frac{n}{2}[-2ne^{-nz} + zn^2e^{-nz}]\right\} + kx + M - \rho g z; \quad (22a)$$

$$\sigma_{zz} = \kappa a_0 + \sum_{n=1}^{\infty} [a_n \cos(nx) + b_n \sin(nx)] \cdot P_t \left\{ [1 + \frac{n}{2} z] e^{-nz} \right\} - \rho g z; \quad (22b)$$

$$\sigma_{xz} = \mu\kappa a_0 + \sum_{n=1}^{\infty} \left[\frac{a_n}{n} \sin(nx) - \frac{b_n}{n} \cos(nx) \right] \cdot P_t \left\{ -[ne^{-nz}] + \frac{n}{2} [e^{-nz} - zne^{-nz}] \right\} - kz. \quad (22c)$$

Solution for overriding thrust sheet (φ_{t3}): fault-bend fold—point load summation

If several point loads are lined up along the upper boundary or surface of the model at some regular interval, l, then the effect of these loads will add up at each point within the model area. Additionally, by inclining these loads, they will have a vertical component and a tangential component (Fig. 4). The stress function for an inclined point load is

$$\varphi_{t3} = \frac{-P_t}{\pi} r\gamma \sin\gamma; \quad (23)$$

where $\gamma = (\theta_l + \pi/2 - \alpha)$, and θ_l and α are defined in Fig. 4. The stresses due to a single point load are

$$\sigma_{xx} = \frac{-2P_t}{\pi} \left[\frac{x^2 z}{r^4} \sin\alpha + \frac{x^3}{r^4} \cos\alpha \right]; \quad (24a)$$

$$\sigma_{zz} = \frac{-2P_t}{\pi} \left[\frac{z^3}{r^4} \sin\alpha + \frac{xz^2}{r^4} \cos\alpha \right]; \quad (24b)$$

$$\sigma_{xz} = \frac{-2P_t}{\pi} \left[\frac{xz^2}{r^4} \sin\alpha + \frac{x^2 z}{r^4} \cos\alpha \right]. \quad (24c)$$

We integrate over the interval that the point loads act ($-l$ to l, Fig. 4) to determine the final equations for the stresses. Adding the components of gravity and tectonic compression, we find

$$\sigma_{xx} = \frac{-P_t}{\pi} \left\{ \sin\alpha \left[\theta_1 - \theta_2 - \frac{(x-l)z}{r_1^2} + \frac{(x+l)z}{r_2^2} \right] + \cos\alpha \left[2ln\left(\frac{r_1^2}{r_2^2}\right) + z^2 \left(\frac{r_2^2 - r_1^2}{r_1^2 r_2^2} \right) \right] \right\} + kx + M - \rho g z; \quad (25a)$$

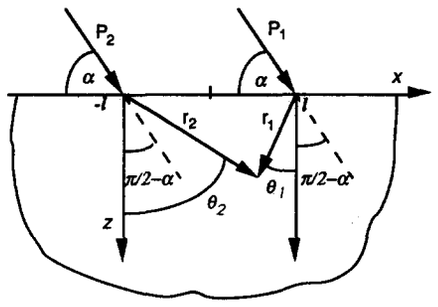

Fig. 4. Angular relations for inclined point loads. Stress function, φ, can be shown to be a function of the load and angular relations.

$$\sigma_{zz} = \frac{-P_t}{\pi} \left\{ \sin\alpha \left[\theta_1 - \theta_2 + \frac{(x-l)z}{r_1^2} - \frac{(x+l)z}{r_2^2} \right] - \cos\alpha \left[z^2 \left(\frac{r_2^2 - r_1^2}{r_1^2 r_2^2} \right) \right] \right\} - \rho g z; \quad (25b)$$

$$\sigma_{xz} = \frac{-P_t}{\pi} \left\{ \cos\alpha \left[\theta_1 - \theta_2 + \frac{(x-l)z}{r_1^2} - \frac{(x+l)z}{r_2^2} \right] - \sin\alpha \left[z^2 \left(\frac{r_2^2 - r_1^2}{r_1^2 r_2^2} \right) \right] \right\} - kz. \quad (25c)$$

Finally, the amount of load applied at each point (P_t) can be varied so that the final distributed load is of the geometric form of a fault-bend fold.

Pore pressure

The hydrostatic pore pressure can be determined at any point within the model by considering the column of rock above that point to be saturated with water. Using a normal hydrostat of 0.01 MPa m^{-1}, which is equivalent to the weight of the column of water, the pore pressure is calculated at every point in the half space. The hydrostat is calculated to include the depth within the half space as well as the added fluid pressure due to the height of the overburden. The effect of pore pressure is to reduce the mean stress at each point following the law of effective stress $\sigma_e = \sigma_n - \sigma_p$; where σ_e is the effective stress, σ_n is the normal stress and σ_p is the pore pressure (e.g. Hubbert & Rubey 1959, Handin *et al.* 1963). The presence of pore pressures does not change the differential stress within the system.

Scaling

The forces and stresses in the lower plate have been scaled to the force resulting from the overriding thrust sheet–synorogenic sedimentary cover. The ratio of the stress due to the overburden to the amount of tectonic compression at $x = 0$, $z = 0$, can be represented as a non-dimensional parameter Π_s. This scaling is done to avoid casting the model in terms of a specific thrust sheet geometry, and therefore yields results that can be adapted for many thrust sheets.

Lengths have been scaled to a distance in the x direction of π. This is chosen since several of the stress functions are periodic over the interval π or 2π. To facilitate comparisons between all the models this length scale is used in all cases. The height of the overriding thrust sheet and the maximum height of the synorogenic sedimentary cover are both taken to be 0.16π (0.5), while the depth of the model area shown is 0.32π (1.0), or twice the height of the overriding thrust sheet. In effect, the models plotted examine the stresses to twice the depth of décollement of the previous thrust sheet. However, the model solution is valid for x and $z \to \infty$, and only a small portion is plotted as the solution. The height of the thrust sheet chosen is strictly arbitrary. The

results of the model are qualitatively the same for a large range of values.

RESULTS OF MODELS

These models were developed to determine the orientation of stress and fault trajectories within the area beneath a ramping thrust sheet. In order to do this, a method of failure for the model has to be assumed. By using a Coulomb criterion for failure, fault trajectories can be drawn oriented relative to the principal stress trajectories at an amount equal to the internal angle of friction. We employ two methods to determine where failure would initiate (Fig. 5). In the first method we choose values for Π_s which result in reasonable looking stress and fracture trajectories using a Coulomb criterion. In these cases Π_s ranges from 1.5 to 4. We then apply a Coulomb criterion at each point in the model using an internal angle of friction (ϕ) of 30°. By starting at a high value of cohesion and reducing it, the cohesion and location of the first point to fail is determined. For the second method, cohesion is chosen as a fraction of the vertical stress due to gravity beneath the thickest portion of the overriding thrust sheet ($0.1P_t$). The regional compressive stress, initially zero, is increased until a portion of the model reaches failure. In both cases, the point of initial failure has approximately the same position, and is always along the surface $z = 0$. Therefore, the method used to determine failure will not affect the results. In the models presented here the first method has been employed.

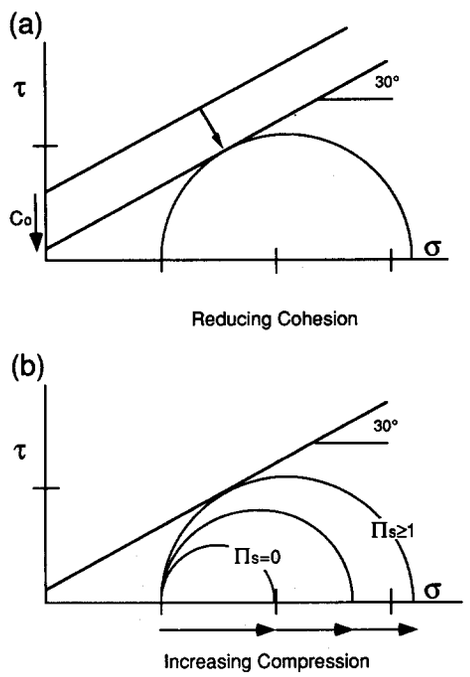

Fig. 5. Mohr circle diagrams showing the two methods employed to determine location of failure within model area. (a) Cohesion (*Co*) starts at some high value and is slowly reduced until the first circle is tangential to the failure envelope. (b) Regional compression, φ_c, is initially zero and is increased until the first circle is tangential to the failure envelope.

For the case of an exponentially decreasing surface load the principal stresses slowly decrease in magnitude to the foreland (right) away from the maximum compressive stress and surface load (Fig. 6a). A counterclockwise change in orientation of the near surface principal stress trajectories results from the interplay between decreasing mean stress (due to decrease in overburden) and decreasing horizontal regional compression. This results in curved fault trajectories in the right or foreland portion of the model (Fig. 6b). The first area to fail is toward the center-right portion of the footwall at the model surface, near $x = 0.6\pi$, $z = 0$ (Fig. 6c). One of the two possible fault trajectories that corresponds to this failure location approximates a flat and ramp geometry. It is subhorizontal beneath the thickest overburden, and curves upward as the overburden thins. The calculated fault trajectories are valid only for the onset of failure, and would represent an actual fault trajectory only if the development of the initial fracture did not greatly affect the stress state. Fault trajectories at greater depths remain subhorizontal due to the increasing importance of body forces with depth.

The orientations of principal stress directions and fracture trajectories are clearly dependent on the ratio of compression to overburden, Π_s (Fig. 7). For the exponentially configured model, as Π_s increases, the predicted fault trajectories rotate (this is true of all three models, but is shown in detail for this model only). Using a cohesion of $0.1P_t$, failure is not reached until $\Pi_s \cong 2$. Therefore, failure occurs in the footwall only after the regional compression builds to the point where it is significantly greater than the weight of the overriding thrust sheet.

Results for the Fourier series fault-bend fold geometry show a higher degree of variability in the orientation of principal stress directions (Fig. 8a). Variation in the magnitude of shear stress with depth affects the orientation of principal stresses and, therefore, fault trajectories (Fig. 8b). However, the results are similar to the exponentially decreasing surface load model. Failure occurs first at the model surface, near the leading edge of the overriding thrust sheet. Even when the geometry of the overriding thrust sheet is varied, failure always occurs at the leading edge of the thrust toe. From the Mohr circle plots for this model we can see that the maximum differential stress occurs at the origin ($x = 0$) and decreases to the right as $x \rightarrow \pi$ (Fig. 8c). The minimum principal stress decreases toward the right and becomes tensile at the surface near $x = 0.6\pi$. It is near this point that failure occurs first ($x \approx 0.7\pi$), indicating that the decrease in mean stress is more significant than the decrease in maximum principal stress.

In the point-load fault-bend fold geometry the principal stresses change orientation in a counter-clockwise sense and diminish in magnitude towards the right or foreland portion of the model (Fig. 9a). The fault trajectories are nearly horizontal beneath the portion of the overriding thrust sheet that has a constant height and

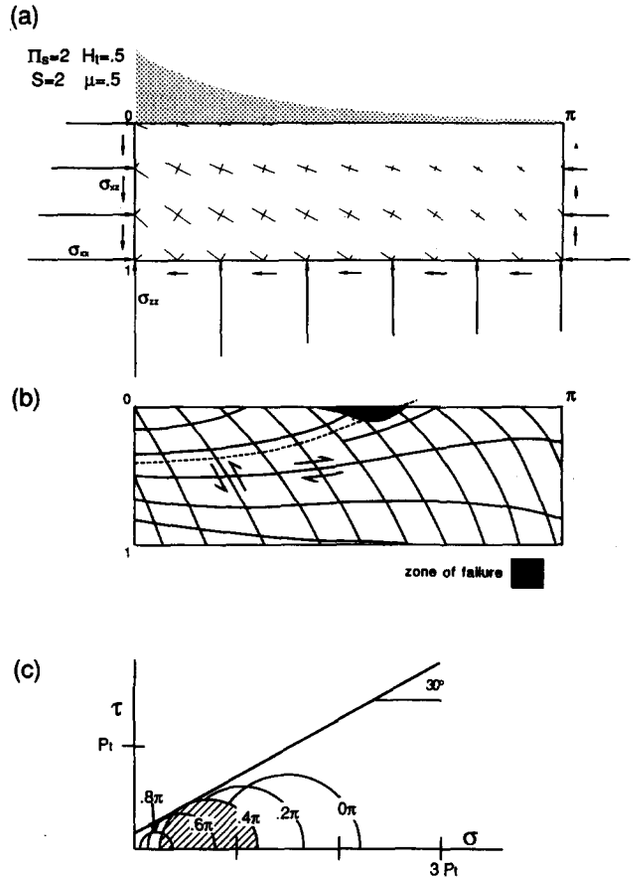

Fig. 6. Summary of models for exponentially decreasing surface load. (a) The configuration of the model showing the surface boundary conditions and the calculated state of stress. The lengths of stress bars external to the model are scaled to half the maximum height of overburden at $x = 0$. Stress bars internal show the relative magnitudes of the principal stresses at each point. (b) Fracture trajectories are determined using a Coulomb criterion and an internal angle of friction of 30°. The shaded area represents the first area that will be in failure for this model. The thrust fault that corresponds is dashed. (c) Mohr circle representation of stress along the surface $z = 0$ shows how the combination of changing mean stress and differential stress interact and result in failure occurring near $x = 0$, $z = 0.5\pi$. Each circle is labeled to correspond to its position along the surface.

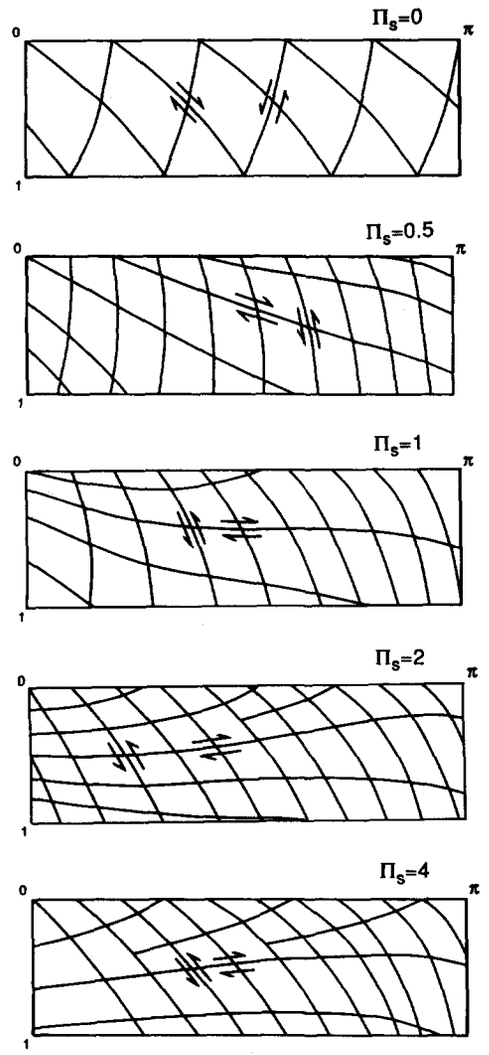

Fig. 7. Series of models showing how increasing the compressional stress, φ_c, affects the orientation of fracture trajectories. Examples are shown ranging from no added regional compression ($\Pi_s = 0$), to regional compression of four times the stress due to the overburden ($\Pi_s = 4$) at $x = 0$, $z = 0$.

curve upward beneath the thinning portion of the thrust toe (Fig. 9b). The state of stress beneath the overriding thrust sheet is directly related to the height of the overburden at that point. States of stress are nearly identical for the points $x = 0, 0.2\pi, 0.4\pi$, while differential stresses are essen tially absent along the surface to the right of the thrust toe ($x = 0.8\pi$ to $x = \pi$) (Fig. 9c). Stresses reach the failure criterion first near the leading edge of the overriding thrust sheet ($x = 0.7\pi$).

The models all share two important results: (1) one of the two predicted fault trajectories generally follows a curved geometry that is nearly horizontal to the left and curves upward to the right; and (2) failure initiates at the model surface well toward the foreland ($x \cong 0.75\pi$) where fracture is favored by the trade-off between the spatial rates at which mean stress and differ ential stress are decreasing toward the foreland. At greater depths the differential and mean stresses are greater, but the general trend of moving toward failure in the foreland region of the model still holds.

Effect of pore pressure

The introduction of a pore fluid causes the mean stress to be reduced by an amount equal to the pore pressure, resulting in an effective stress state. Areas beneath a thick overburden experience a greater reduction of mean stress than areas beneath a thin overburden. This effect is shown for the models of an exponentially thinning surface load and for the point-load fault-bend fold (Fig. 10). For the exponential thinning load, where the surface slope is particularly large (Fig. 6a), the stress state at the point $x = 0$, $z = 0$ experiences the largest effect of added pore pressure ($\sigma_e \ll \sigma_n$), and points more toward $x = \pi$ have relatively small reductions in the mean stress ($\sigma_e \cong \sigma_n$). For this model, failure is now predicted to initiate at the point $x = 0$, $z = 0$ (Fig. 10a). The effect of pore pressure on the location of failure within the point-loaded fault-bend fold model, although shifted to the left (i.e. toward $x = 0$), still occurs well out under the overburden at $\sim 0.4\pi$ (Fig. 10b). The pre-

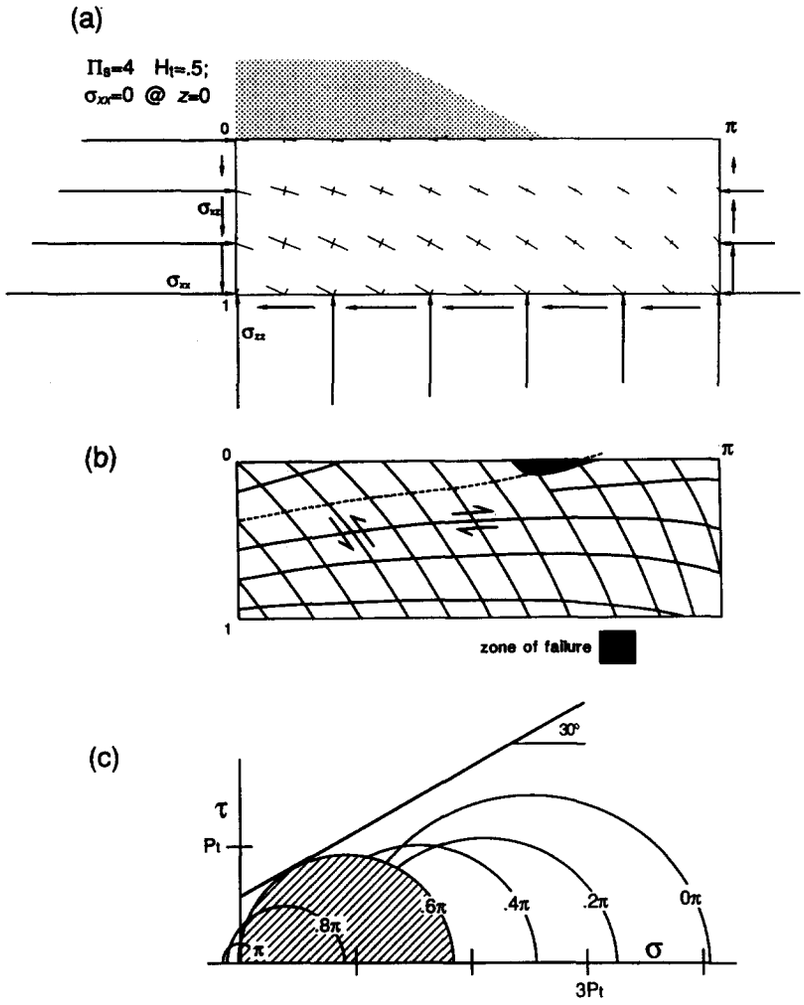

Fig. 8. Summary of models for fault-bend fold surface load modelled by a Fourier series. (a) Configuration of the model showing the boundary conditions and the calculated state of stress. (b) Fracture trajectories. Area predicted to fail first is shaded. The thrust fault that corresponds is dashed. (c) Mohr circle representation of stress showing failure occurring near $x = 0$, $z = 0.6\pi$.

dicted fracture trajectories are unaltered by the addition of pore pressure.

At depth within both of these models, an effective stress state exists that is closer overall to failure than the case without pore pressure. That is to say that the total range of mean stress throughout the model is reduced. However, the prediction that failure would occur at the surface first remains unchanged.

GEOLOGIC IMPLICATIONS

The intent of these models is to study that part of foreland thrust belts for which we have the most geologic constraints and for which our model assumptions are most appropriate. For instance, in the Idaho–Wyoming–Utah thrust belt, the most external thrust sheets are the best constrained in terms of the stratigraphy, level of décollement and timing of emplacement (Armstrong & Oriel 1965, Royse *et al.* 1977, Dixon 1982, Wiltschko & Dorr 1983). In addition, these thrust sheets have simple deformation histories as compared to the more internal sheets in the belt. These models are most appropriate for the more external portions of any particular thrust belt because of the use of a Coulomb failure criterion. In areas where the primary behavior of the entire stratigraphic section is macroscopically ductile this assumption would not be appropriate. The following geologic interpretations, therefore, are meant to apply to the external portions of orogenic belts.

Location of fault nucleation

One of the more interesting results of these models is that failure occurs first at the model surface. We suggest, then, that thrust faults do not propagate along a basal décollement and then ramp at some point, but rather that they nucleate at or near the top of the mechanically continuous stratigraphic sequence. In the Idaho–Wyoming–Utah thrust belt, for example, the synorogenic sediments are thicker than the strong unit that they cover. Therefore, fault propagation may initiate near the top of the strong unit and propagate upwards as blind thrusts and downwards into the basal décollement. This is consistent with observations of fault displacement patterns made by Ellis & Dunlap (1988) who argue that faults nucleate at some distance above a décollement plane and propagate both downward and upward with

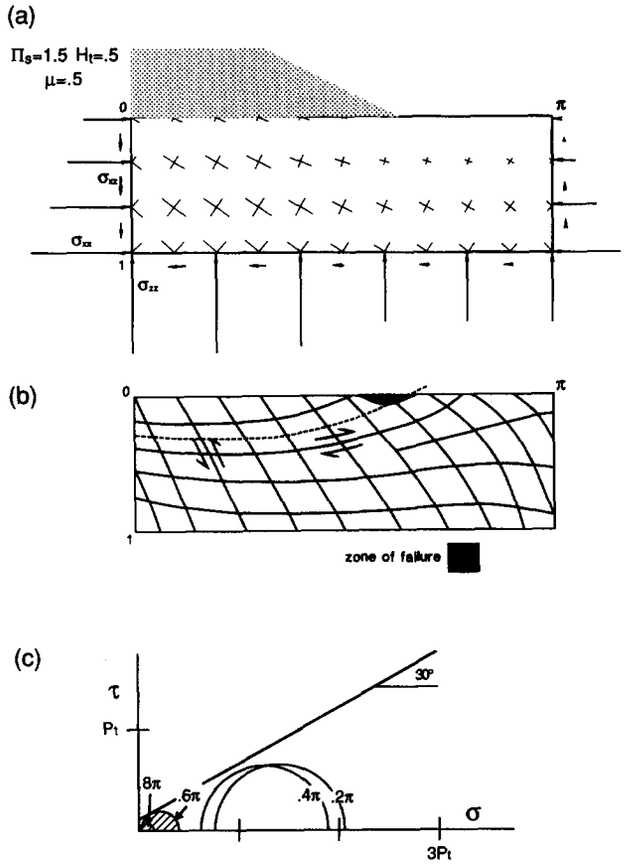

Fig. 9. Summary of models for fault-bend fold geometry represented by inclined point loads summed over the interval shown. (a) Configuration of the model showing the boundary conditions and the calculated state of stress. (b) Fracture trajectories. Area predicted to fail first is shaded. The thrust fault that corresponds is dashed. (c) Mohr circle representation of stress showing failure occurring near $x = 0$, $z = 0.6\pi$.

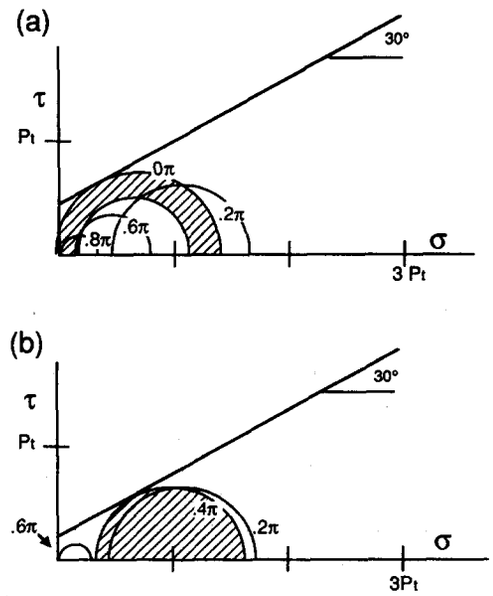

Fig. 10. State of stress, including the effect of pore pressure, for the models of an (a) exponentially decreasing surface load and a (b) point-loaded fault-bend fold geometry. In both cases the point which is predicted to fail first moves toward $x = 0$.

time. Also, Eisenstadt & De Paor (1987) propose a sequence of failure in which ramps form first at shallow levels, and grow upward and downward by capturing flats between independently formed ramp segments.

Another important aspect of our models is that thrust faults nucleate at or near the leading edge of the overriding thrust sheet or where the synorogenic sedimentary cover is sufficiently thin. The weight of the overriding thrust sheet–synorogenic cover stabilizes the footwall due to the large increase of mean stress (Figs. 6c, 8c and 9c). Therefore, the location of the new thrust fault forming within the footwall will be directly controlled by the length and mass of the overriding thrust sheet and/or synorogenic cover. Thrust initiation occurring beneath the leading edge of the overriding thrust sheet is in general agreement with our initial results (Goff & Wiltschko 1986, 1989) and those of Panian & Pilant (1990).

The introduction of a hydrostatic pore pressure to the system will move the location at which failure is predicted toward the hinterland. The distance this failure point is shifted is a function of the taper of the overburden. If there is a large taper above the point at which failure is predicted to occur without pore pressures, there will be a large shift of this point when pore pressure is introduced. If there is no taper, failure is predicted to occur at the same point for both the cases of no pore pressure and hydrostatic pore pressure.

The inclusion of an overpressured horizon (where fluid pressures exceed hydrostatic) within the stratigraphic column would probably result in 'weakening' that horizon such that it would fail before any other. For example, the rapid loading of the footwall during the emplacement of a thrust sheet may dramatically compact shales and other clastics beneath the overrriding thrust sheet. Fluid pressures may increase to above hydrostatic, and even perhaps exceed normal stresses. This would occur where there is the greatest loading rate relative to hydraulic conductivity on the footwall strata. However, it may be difficult to explain the systematic character of thrust–ramp spacing and climb of the décollement within a thrust belt in terms of overpressured horizons alone (Gretener 1979). Additionally, evidence from the southern portion of the Wyoming thrust belt and the southern Pyrenees suggests that there may not be a rapid loading of the footwall, especially if erosion is balancing uplift and thrust sheet emplacement (Warner & Royse 1987, De Paor & Anastasio 1987).

Fault trajectories

The fault trajectories predicted by using a simple Coulomb criterion ($\phi = 30°$) consist of a 'flat' or subhorizontal portion beneath the thickest portion of the overburden, with a 'ramp' or inclined portion to the foreland of the model, where the overburden decreases in height. This pattern is consistent with the geometry of large thrusts. Comparison of the curved 'ramp and flat' geometry predicted here with previous models of compressional regimes (Hafner 1951, Mandl & Shippam 1981) in

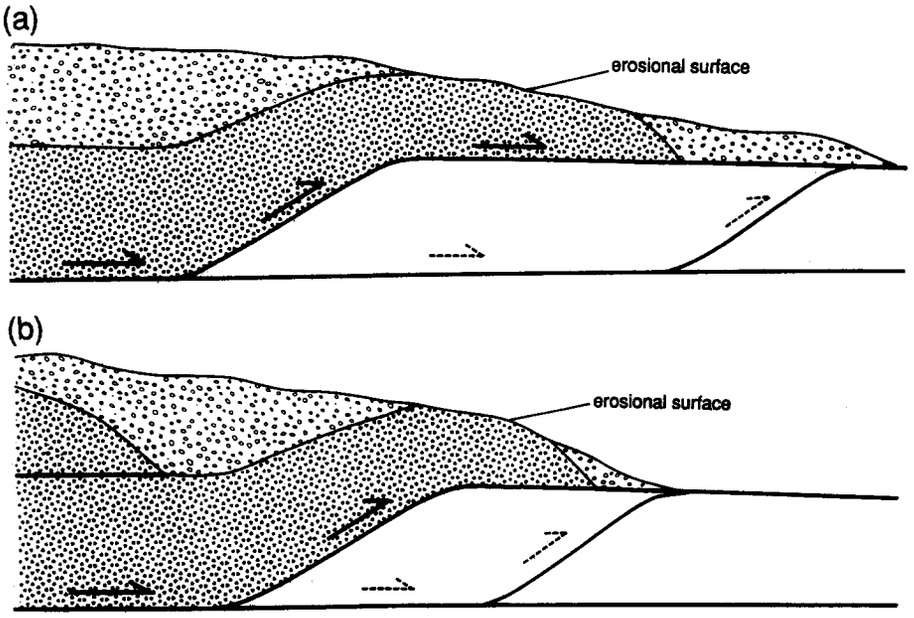

Fig. 11. Relationship of thrust sheet spacing and the formation of the 'next' thrust ramp to the time when the stresses in the footwall thrust sheet are sufficient to cause failure. (a) Failure stresses are reached after large transport, or due to the emplacement of a large overriding thrust sheet. (b) Failure stresses are reached after small transport, or due to the emplacement of a small or thin thrust sheet.

which fault trajectories are inclined upward throughout the model suggests that the effect of overburden on the stress state within foreland thrust belts is an important feature.

Comparison with fault spacing data

One of the goals of this study is to explain the systematic spacing of thrust sheets (Fig. 1). Since the next frontal ramp would nucleate near the toe of the last thrust sheet, how can we explain thrust belts that are comprised of tightly imbricated thrust sheets (e.g. Sawtooths of Montana, Mudge 1982), while others have more widely spaced thrust faults (e.g. southern Appalachians, Woodward 1985)? Two factors may ultimately control thrust-ramp spacing: (1) the displacement history of the previously formed thrust sheet; and (2) the rate of emplacement and uplift of thrust sheet relative to the rate of erosion and sediment delivery to the sedimentary cover. Both of these processes would affect the size and distribution of material over the footwall thrust sheet, which our model predicts to be the most important parameter in determining thrust–ramp spacing. If a particular thrust sheet is displaced a large distance along a fault before failure in the footwall occurs, we might expect the spacing between thrust sheets to be relatively large (Fig. 11a). If there is only a small amount of displacement before footwall failure, then there might be a relatively small spacing between thrust sheets (Fig. 11b). Additionally, the effect on the stresses in the footwall will be significantly different depending on the rates of delivery and removal of sediments from the front of the advancing thrust sheet. Fast removal rates should result in closely spaced thrust faults (less overburden), while large sediment accumulations (slow removal rates) should increase the spacing between frontal ramps (more overburden). Our models also predict a natural tendency for each successive thrust sheet to be thinner than the last one to form. A consequence of this thinning is the decrease in spacing of successive frontal ramps as well as the stepping up of the décollement level to the foreland.

Exceptions to these predictions may occur, however. By not including a weak horizon within these models, the location of the basal décollement and the thickness of the footwall thrust sheet are not predetermined. Presumably, the fault trajectory that links up to the initial failure zone would be the most likely fault to form. In addition, these models ignore the pre-existing stratigraphic taper typical of foreland basins. On the basis of force balance arguments alone, one may expect that the length of each thrust sheet will decrease as the stratigraphic section of the thrust belts thins, as has been shown by other studies (Bombolakis 1986).

Deformation history of a thrust belt

The models, as presented, look at the state of stress in the footwall beneath a ramping thrust. Implicit in our models is a thrust sheet and synorogenic sedimentary cover that exerts a load on the footwall during the subsequent deformation history. Yet, what mechanism was responsbile for the emplacement of the 'first' thrust sheet? The internal portions of thrust belts are frequently described as 'mobile' or ductile. As in the case of the Alps, the core of many mountain belts are frequently highly metamorphosed, and show much higher body strains than the more external portions of the orogen (Bernoulli *et al.* 1974). Ignoring details of how the deformation occurs in the internal portions of thrust belts, this deformation causes thickening of the lithosphere, uplift and erosion, and the development of a

synorogenic sedimentary cover. If these deposits extend over a great distance into the developing foredeep, but remain mechanically detached from the more lithified shelf deposits, they would act similarly to the synorogenic sedimentary cover modelled here. The vertical load due to a synorogenic sedimentary cover is just as significant as the load due to an overriding thrust sheet of equal mass and dimension. Therefore, within a thrust belt, the size of the first brittle thrust sheet to form may be controlled by the presence of a regional scale, relatively unlithified and mechanically separated sedimentary cover. Once the first thrust sheet forms the combination of the effects of the interaction of thrust sheets and the development of synorogenic sediments may control the stress state in the footwall of each succeeding thrust sheet.

CONCLUSIONS

The observation that thrust ramps are spaced systematically in many thrust belts suggests that a mechanical process controls frontal ramp formation. In this study we investigate one aspect which may be important in this process, the effect of the emplacement of hanging wall thrust sheets and the development of a synorogenic sedimentary cover on the state of stress in the footwall. This analysis leads to several implications concerning the development of frontal ramps and flats.

An overriding thrust sheet or advancing sedimentary cover causes the underlying footwall to be relatively stable with respect to failure using a Coulomb failure criterion. This is a result of the increase in mean stress due to additional overburden. The increase in mean stress counteracts the effect of higher horizontal compression in the hinterlandward portions of the footwall. Therefore, there is a trade off between the spatial rates at which mean stress and differential stress decrease toward the foreland which controls the location of initial failure within the footwall.

Failure is found to initiate at the model surface, stepped out well away from the thickest portions of the overriding thrust sheet–synorogenic sedimentary cover. The fracture trajectory predicted for these models in general follows a curved flat and ramp geometry, such that the fault trajectory is subhorizontal beneath the overriding thrust sheet and curves upward beneath the thinning thrust toe. The models suggest that thrust faults may form when a frontal ramp nucleates near the top of the strong or mechanically continuous portion of the stratigraphic section but beneath the weaker or mechanically detached synorogenic sediments or overriding thrust sheet. The development of a 'brittle style' thrust belt, and specifically the hinterlandward-most thrust sheet, may be controlled by the presence of synorogenic sediments which are shed off the more mobile internal portions of the orogenic belt.

The presence of a fluid at hydrostatic pressure will cause a shift of the point of predicted failure toward the hinterland. In the case where the taper of the overburden is low this shift will be small. Therefore, for foreland fold-and-thrust belts, if the taper of the overburden at the thrust front is small, hydrostatic pore presures will only slightly alter the predicted location of initial failure.

The spacing of thrust sheets may be controlled by the combination of thrust displacement and sedimentary cover development. If the displacement and cover are small then we might expect a small spacing of thrust sheets. However, if there is significant displacement of the hanging wall or a large sedimentary cover formed before footwall failure, there might be a large spacing of thrust ramps.

Finally, although the exact dimensions of each thrust sheet within a thrust belt cannot be predicted by these models, it is shown that each successive thrust sheet would be thinner toward the foreland, even if there were no stratigraphic taper to the deforming section. This may be an additional explanation for why décollement levels tend to climb to the foreland in most thrust belts.

Acknowledgements—This work was supported in part by the Center for Tectonophysics at Texas A&M University and ARCO Oil and Gas Company. This paper is based on portions of a Ph.D. dissertation (Goff 1990) completed at Texas A&M. Reviews and comments on that work by Gregg Erickson, Ted Apotria, Ray Fletcher, Melvin Friedman, Andreas Kronenberg, and John Spang are all gratefully acknowledged. Two anonymous reviews and comments by Steven Wojtal helped to tighten the final version and are greatly appreciated.

REFERENCES

Anderson, E. M. 1942. *The Dynamics of Faulting*. Oliver and Boyd, London.

Armstrong, F. C. & Oriel, S. S. 1965. Tectonic development of Idaho–Wyoming thrust belt. *Bull. Am. Ass. Petrol. Geol.* **71**, 1847–1866.

Bally, A. W., Gordy, P. L. & Stewart, G. A. 1966. Structure, seismic data, and orogenic evolution of the southern Canadian Rocky Mountains. *Can. Petrol. Geol.* **14**, 337–381.

Bernoulli, D., Laubscher, H. P., Trumpy, R. & Wenk, E. 1974. Central Alps and Jura Mountains. In: *Mesozoic–Cenozoic Orogenic Belts* (edited by Spencer, A. W.). *Spec. Publs geol. Soc. Lond.* **4**, 85–108.

Bombolakis, E. G. 1986. Thrust-fault mechanics and origin of a frontal ramp. *J. Struct. Geol.* **8**, 281–290.

Bombolakis, E. G. 1989. Thrust fault mechanics and dynamics during the developmental stage of a foreland belt. *J. Struct. Geol.* **11**, 439–455.

Cello. G. & Nur, A. 1988. Emplacement of foreland thrust systems. *Tectonics* **7**, 261–272.

De Paor, D. G. & Anastasio, D. J. 1987. The Spanish External Sierra: a case history in the advance and retreat of mountains. *Nat. Geograph. Res.* **3**, 199–209.

Dixon, J. S. 1982. Regional synthesis, Wyoming salient of the Western Overthrust Belt. *Bull. Am. Ass. Petrol. Geol.* **66**, 1560–1580.

Eisenstadt, G. & De Paor, D. G. 1987. Alternative model of thrust-fault propagation. *Geology* **15**, 630–633.

Ellis, M. A. & Dunlap, W. J. 1988. Displacement variation along thrust faults: implications for the development of large faults. *J. Struct. Geol.* **10**, 183–192.

Goff, D. 1990. Mechanics of thrust-ramp spacing. Unpublished Ph.D. dissertation, Texas A&M University.

Goff, D. & Wiltschko, D. V. 1986. Analytical models of the stresses within the lower plate in front of a ramping thrust sheet. *Geol. Soc. Am. Abs. w. Prog.* **18**, 616.

Goff, D. & Wiltschko, D. V. 1989. Stresses beneath ramping thrusts: implications for fault nucleation. *EOS* **70**, 1367.

Gretener, P. E. 1972. Thoughts on overthrust faulting in a layered sequence. *Can. Petrol. Geol.* **20**, 583–607.

Gretener, P. E. 1979. Pore pressure: fundamentals, general ramifications, and implications for structural geology (revised). *Am. Ass. Petrol. Geol., Educ. Course Note Series* **4**.
Hafner, W. 1951. Stress distribution and faulting. *Bull. geol. Soc. Am.* **62**, 373–398.
Handin, J., Hager, R. V., Friedman, M. & Feather, J. 1963. Experimental deformation of sedimentary rocks under confining pressure: pore pressure tests. *Bull. Am. Ass. Petrol. Geol.* **47**, 717–755.
Hubbert, M. K. & Rubey, W. W. 1959. Role of pore pressure in mechanics of overthrust faulting—I. Mechanics of fluid-filled porous solids and its application to overthrust faulting. *Bull. geol. Soc. Am.* **70**, 115–166.
Jacobeen, F., Jr & Kanes, W. H. 1974. Structure of the Broadtop synclinorium and its implication for Appalachian structural style. *Bull. Am. Ass. Petrol. Geol.* **58**, 362–375.
Jacobeen, F., Jr & Kanes, W. H. 1975. Structure of Broadtop synclinorium, Wills Mountain anticlinorium, and Allegheny frontal zone. *Bull. Am. Ass. Petrol. Geol.* **59**, 1136–1150.
Jones, B. 1971. Folded faults and sequence of thrusting in Alberta foothills. *Bull. Am. Ass. Petrol. Geol.* **55**, 292–306.
Kraig, D. H., Wiltschko, D. V. & Spang, J. H. 1987. Interaction of basement uplift and thin-skinned thrusting, Moxa arch and the Western Overthrust Belt, Wyoming: a hypothesis. *Bull. geol. Soc. Am.* **99**, 654–662.
Kulander, B. R. & Dean, S. L. 1986. Structure and tectonics of central and southern Appalachian Valley and Ridge and Plateau provinces, West Virginia and Virginia. *Bull. Am. Ass. Petrol. Geol.* **70**, 1674–1684.
Lamerson, P. R. 1982. The Fossil Basin and its relationship to the Absaroka thrust system, Wyoming and Utah. In: *Geologic Studies of the Cordilleran Thrust Belt* (edited by Powers, R. B.). *Rocky Mountain Ass. Geol.* **1**, 279–340.
Lawrence, D. T., Doyle, M. & Aigner, T. 1990. Stratigraphic simulation of sedimentary basins: concepts and calibrations. *Bull. Am. Ass. Petrol. Geol.* **74**, 273–295.
Mandl, G. & Shippam, G. K. 1981. Mechanical model of thrust sheet gliding and imbrication. In: *Thrust and Nappe Tectonics* (edited by McClay, K. R. & Price, N. J.). *Spec. Publs geol. Soc. Lond.* **9**, 79–98.
Mudge, M. R. 1982. A resume of the structural geology of the northern disturbed belt northwestern Montana. In: *Geologic Studies of the Cordilleran Thrust Belt* (edited by Powers, R. B.). *Rocky Mountain Ass. Geol.* **1**, 91–122.
Panian, J, & Pilant, W. 1990. A possible explanation for foreland thrust propagation. *J. geophys. Res.* **86**, 8607–8615.
Perry, W. J. 1978. Sequential deformation in the central Appalachians. *Am. J. Sci.* **278**, 518–542.
Platt, J. P. 1988. The mechanics of frontal imbrication, a first-order analysis. *Geol. Rdsch.* **77**, 577–589.
Pollard, D. D. & Johnson, A. M. 1973. Mechanics of growth of some laccolithic intrusions in the Henry Mountains, Utah, II. Bending and failure of overburden layers and sill formation. *Tectonophysics* **18**, 311–354.
Price, R. A. 1981. The Cordilleran foreland thrust and fold belt in the southern Canadian Rocky Mountains. In: *Thrust and Nappe Tectonics* (edited by McClay, K. R. & Price, N. J.). *Spec. Publs geol. Soc. Lond.* **9**, 427–448.
Royse, F., Warner, M. A. & Reese, D. L. 1975. Thrust belt structural geology and related stratigraphic problems Wyoming–Idaho–Northern Utah. In: *Deep Drilling Frontiers of the Central Rocky Mountains* (edited by Bolyard, D. W.). *Rocky Mountain Ass. Geol.*, 41–54.
Rubey, W. W. & Hubbert, M. K. 1959. Role of pore pressure in mechanics of overthrust faulting—II. Overthrust belts in geosynclinal area of western Wyoming in light of fluid-pressure hypothesis. *Bull. geol. Soc. Am.* **70**, 167–206.
Schmidt, C. J. & Perry W. J. (editors) 1988. *Interaction of the Rocky Mountain Foreland and the Cordilleran Thrust Belt. Mem. geol. Soc. Am.* **171**.
Suppe, J. 1980. A retrodeformable cross section of northern Taiwan. *Proc. geol. Soc. China (Taiwan)* **23**, 46–55.
Thomas, W. A. 1985. Chapter IV—Northern Alabama Sections. In: *Valley and Ridge Thrust Belt. Balanced Structural Sections; Pennsylvania to Alabama* (edited by Woodward, N. B.). *Appalachian Basin Industrial Associates, Univ. Tennessee Dept Geol. Sci., Studies in Geol.* **12**, 54–61.
Timoshenko, S. P. & Goodier, J. N. 1970. *Theory of Elasticity* (3rd edn). McGraw-Hill, New York.
Warner, M. A. & Royse, F. 1987. Thrust faulting and hydrocarbon generation: Discussion. *Bull. Am. Ass. Petrol. Geol.* **71**, 882–889.
Wiltschko, D. V. & Dorr, J. A. 1983. Timing and deformation in overthrust belt and foreland of Idaho, Wyoming, and Utah. *Bull. Am. Ass. Petrol. Geol.* **67**, 1304–1322.
Wiltschko, D. V. & Eastman, D. B. 1983. Role of basement warps and faults in localizing thrust fault ramps. In: *Contributions to the Tectonics and Geophysics of Mountain Chains* (edited by Hatcher, R. D., Jr, Williams, H. & Zietz, I.). *Mem. geol. Soc. Am.* **158**, 177–190.
Wiltschko, D. V. & Eastman, D. B. 1988. A photoelastic study of the effects of preexisting reverse faults in basement on the subsequent deformation of the cover. In: *Interaction of the Rocky Mountain Foreland and the Cordilleran Thrust Belt* (edited by Schmidt, C. J. & Perry, W. J.). *Mem. geol. Soc. Am.* **171**, 111–118.
Woodward, N. B. (editor) 1985. *Valley and Ridge Thrust Belt: Balanced Structural Sections; Pennsylvania to Alabama. Appalachian Basin Industrial Associates, Univ. Tennessee Dept Geol. Sci., Studies in Geol.* **12**.
Woodward, N. B. 1988. Primary and secondary basement controls on thrust sheet geometries. In: *Interaction of the Rocky Mountain Foreland and the Cordilleran Thrust Belt* (editors Schmidt, C. J. & Perry, W. J.). *Mem. geol. Soc. Am.* **171**, 353–366.
Woodward, N. B. & Rutherford, E., Jr. 1989. Structural lithic units in external orogenic zones. *Tectonophysics* **158**, 247–267.
Wright, L. D. & Coleman, J. M. 1974. Mississippi River mouth processes: effluent dynamics and morphological development. *J. Geol.* **82**, 751–758.

APPENDIX

To model the stresses beneath a fault-bend fold geometry, a Fourier series has been developed to represent the hanging wall geometry of a thrust sheet (Fig. A1). The geometry of the series is scaled to a height of 1 and then multiplied by the height of the thrust sheet needed for the model. From a drawing of the geometry, the values of $a0$, an and bn are determined using the Euler equations, where:

$$a_0 = \frac{1}{4\pi}[l_1 - l_2 + l_3 - l_4] \tag{A1}$$

$$a_n = \frac{1}{n^2\pi}\left[\frac{\cos(nl_2) - \cos(nl_1)}{(l_2 - l_1)} + \frac{\cos(nl_3) - \cos(nl_4)}{(l_4 - l_3)}\right] \tag{A2}$$

$$b_n = \frac{1}{n^2\pi}\left[\frac{\sin(nl_2) - \sin(nl_1)}{(l_2 - l_1)} + \frac{\sin(nl_3) - \sin(nl_4)}{(l_4 - l_3)}\right]. \tag{A3}$$

The values for a_0, a_n and b_n are substituted into the equation for the Fourier series:

$$f(x) = a_0 + \sum_{n=1}^{\infty} [a_n \cos(nx) + b_n \sin(nx)]. \tag{A4}$$

Finally, by multiplying (A4) by the load, the expression for the stress along the surface of the model is derived:

$$\sigma_{zz} = \left\{a_0 + \sum_{n=1}^{\infty} [a_n \cos(nx) + b_n \sin(nx)]\right\} P_t \text{ at } x = 0. \tag{A5}$$

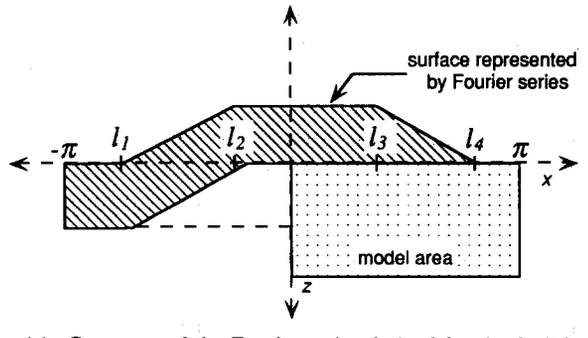

Fig. A1. Geometry of the Fourier series derived for the fault-bend fold models. The points (l_n) can be moved so that the size of the overriding thrust sheet can be varied with respect to the model area.